ZEOLITE STRUCTURE

Three-dimensional inhomogeneity of zeolite structure and composition revealed by electron ptychography

Hui Zhang[1,2,3]*†, Guanxing Li[3]†, Jiaxing Zhang[4], Daliang Zhang[5,6], Zhen Chen[7], Xiaona Liu[8], Peng Guo[8], Yihan Zhu[9,10], Cailing Chen[3], Lingmei Liu[5,6], Xinwen Guo[4], Yu Han[3]*

Structural and compositional inhomogeneity is common in zeolites and considerably affects their properties. Thickness-limited lateral resolution, lack of depth resolution, and electron dose-constrained focusing limit local structural studies of zeolites in conventional transmission electron microscopy (TEM). We demonstrate that a multislice ptychography method based on four-dimensional scanning TEM (4D-STEM) data can overcome these limitations. Images obtained from a ~40-nanometer-thick MFI zeolite exhibited a lateral resolution of ~0.85 angstrom that enabled the identification of individual framework oxygen (O) atoms and the precise determination of the orientations of adsorbed molecules. Furthermore, a depth resolution of ~6.6 nanometers allowed probing of the three-dimensional distribution of O vacancies, as well as the phase boundaries in intergrown MFI and MEL zeolites. The 4D-STEM ptychography can be generally applied to other materials with similar high electron-beam sensitivity.

Zeolites are aluminosilicate microporous crystals with regular intracrystalline cavities and channels of molecular dimensions. The molecular sieving ability of zeolites renders highly desirable size and shape selectivity for adsorption, separation, and catalysis (*1*–*4*). However, the complexity of zeolite structures makes them prone to structural and compositional inhomogeneity that can profoundly affect their properties. For example, the precursors and synthetic conditions affect the location and distribution of functional sites (such as Al pairs and heteroatoms) in the zeolite framework (*5*). Postsynthesis calcination generates oxygen (O) vacancies to render Lewis acid sites in an uncontrolled manner (*6*, *7*). The intergrowth of multiple polymorphs and various phases is common in zeolite crystals (*8*–*10*). The prevalence of inhomogeneity explains why zeolites with the same topology and composition prepared from different batches often exhibit variability in applications (*11*, *12*).

Although inhomogeneity in zeolites has been widely recognized, the precise determination of the related local nonperiodic structures remains challenging given the lack of suitable characterization techniques. For instance, the electron-beam sensitivity of zeolites limits the use of transmission electron microscopy (TEM) to study their structures (*13*–*15*) because the low-electron doses required to prevent structural damage to zeolites often result in images with limited resolution and poor signal-to-noise ratios. New imaging methods that use electron doses more efficiently are needed to mitigate this issue (*16*, *17*).

Among emerging low-dose TEM techniques, integrated differential phase-contrast scanning TEM (iDPC-STEM) has proven effective for imaging zeolite structures, especially for studying guest species located in the micropores (*18*–*20*). Despite the demonstrated successes, iDPC-STEM has limitations. First, the image resolution of iDPC-STEM is severely limited by the specimen thickness. For zeolites, iDPC-STEM can only resolve framework T atoms (where T is Si or Al) (strictly speaking, atomic columns) but not the O atoms between them unless the specimen thickness is within a few unit cells (<10 nm), which is extremely rare in actual samples. Second, like other conventional TEM imaging modes, iDPC-STEM lacks resolving power along the projection direction and cannot identify longitudinal structural inhomogeneity inside the specimen. Third, iDPC-STEM requires precise focusing of the electron beam to achieve high resolution, which could lead to a lower success rate for beam-sensitive materials because structural damage may occur during the fine-tuning of the focus.

Here, we demonstrate that electron ptychography (*21*–*26*) can address these problems and achieve subangstrom resolution to resolve individual O atomic columns in various zeolites with specimen thicknesses up to ~40 nm, which has not been reported with other direct-imaging techniques. Electron ptychography is a coherent diffractive imaging method that uses a series of convergent-beam electron diffraction patterns, commonly referred to as four-dimensional STEM (4D-STEM) data, to generate high-resolution images. The identification of O atoms enabled a semiquantitative analysis of the three-dimensional (3D) distribution of O vacancies throughout the zeolite specimen. Furthermore, 4D-STEM ptychography provided ~6.6-nm depth resolution to reveal the growth mode of MEL zeolite domains along the *b* axis of the MFI zeolite. In addition, acquiring a 4D-STEM ptychography dataset did not require precise focusing of the electron probe, which considerably improved the efficiency of obtaining atomic-resolution phase-contrast images of zeolites and other beam-sensitive materials.

Comparison of iDPC-STEM and 4D-STEM ptychography

Image simulations were first performed to demonstrate the superiority of 4D-STEM ptychography over iDPC-STEM, the state-of-the-art technique for zeolite imaging. A series of 4D-STEM datasets were simulated for [010]-projected zeolite ZSM-5 by varying the specimen thicknesses and convergence angles (see materials and methods for details). Ptychography and iDPC-STEM images were calculated from each dataset. Regardless of the convergence angle, when the sample thickness exceeded 12 nm, iDPC-STEM images started to deviate from the structural model and became difficult to interpret. By contrast, ptychography images were robust, displaying substantial tolerance for variation of up to 40 nm in specimen thickness (Fig. 1A and fig. S1).

We verified the advantage of ptychography experimentally using specially synthesized ZSM-5 zeolite crystals. These ZSM-5 crystals had a highly uniform thickness of 30 to 40 nm along the *b* axis, as evidenced by multiple characterizations (fig. S2), which allowed a reasonable comparison between iDPC-STEM and ptychography. The iDPC-STEM images were acquired using conditions optimized for zeolite imaging (convergence

---

[1]Electron Microscopy Center, South China University of Technology, Guangzhou 510640, China. [2]School of Emergent Soft Matter, South China University of Technology, Guangzhou 510640, China. [3]Advanced Membranes and Porous Materials Center, Physical Science and Engineering Division, King Abdullah University of Science and Technology (KAUST), Thuwal 23955-6900, Saudi Arabia. [4]State Key Laboratory of Fine Chemicals, Frontiers Science Center for Smart Materials, School of Chemical Engineering, Dalian University of Technology, Dalian 116024, China. [5]Multi-scale Porous Materials Center, Institute of Advanced Interdisciplinary Studies, Chongqing University, Chongqing 400044, China. [6]School of Chemistry and Chemical Engineering, Chongqing University, Chongqing 400044, China. [7]School of Materials Science and Engineering, Tsinghua University, Beijing 100084, China. [8]National Engineering Research Center of Lower-Carbon Catalysis Technology, Dalian National Laboratory for Clean Energy, Dalian Institute of Chemical Physics, Chinese Academy of Sciences, Dalian 116023, China. [9]Center for Electron Microscopy, State Key Laboratory Breeding Base of Green Chemistry Synthesis Technology and College of Chemical Engineering, Zhejiang University of Technology, Hangzhou 310014, China. [10]Institute for Frontier and Interdisciplinary Sciences, Zhejiang University of Technology, Hangzhou 310014, China.
***Corresponding authors. Email: hui.materials.zhang@gmail.com (H.Z.); yu.han@kaust.edu.sa (Y.H.)** †These authors contributed equally to this work.

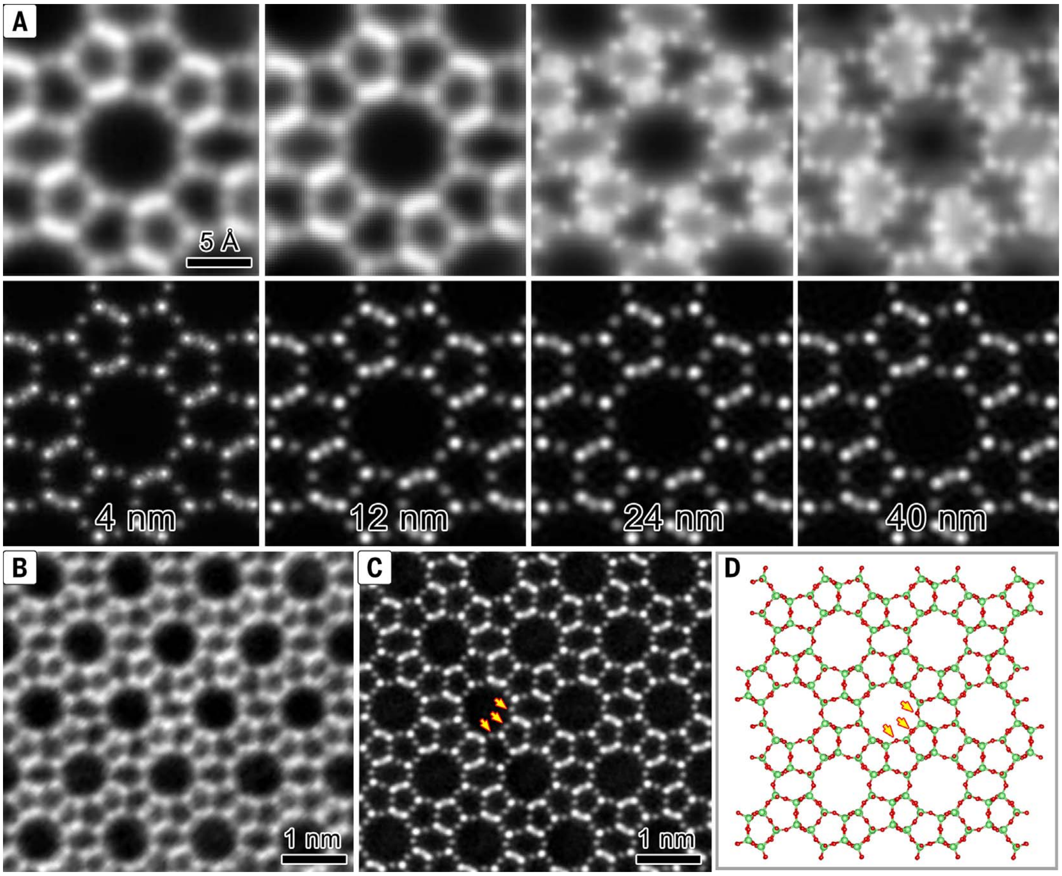

Fig. 1. Comparison of iDPC-STEM and 4D-STEM ptychography. (**A**) Simulated iDPC-STEM (top) and 4D-STEM ptychography (bottom) images of ZSM-5 along the [010] axis with varying thicknesses, as indicated, under a convergence semiangle of 15 mrad. (**B**) iDPC-STEM image of ZSM-5 along the [010] axis, with a specimen thickness of ~10 nm. (**C**) 4D-STEM ptychography image of ZSM-5 along the [010] axis, with a specimen thickness of ~40 nm. (**D**) The [010]-projected structural model of ZSM-5. The yellow arrows in (C) and (D) indicate several O atomic columns in the framework, which are not resolved in (B).

semiangle: 15 mrad; probe current: 2 pA; dwell time: 10 μs; pixel size: 0.380 Å by 0.380 Å), with a total electron dose of ~900 $e^-/Å^2$. The 4D-STEM datasets were collected by using a high-performance hybrid electron microscope pixel array detector (EMPAD) with a probe current of ~0.09 pA, scan step of 0.399 Å, and 256-by-256 probe positions. Limited by the EMPAD frame rate (1000 frames/s), the specimen was subjected to an electron dose of ~3500 $e^-/Å^2$ during data acquisition. However, this dose was still low enough to preserve the structure of ZSM-5. The iterative ptychographic reconstruction used the maximum likelihood (ML) method to update the exit wave function and the linear least squares (LSQ) method to update the object and probe functions (*27*, *28*). Multislice (*29*) and mixed-state (*30*) algorithms were implemented to address the multiple scattering associated with thick specimens and the partial incoherence of electron probes, respectively. Successful reconstruction at low-dose conditions relies on the best possible initial guess for the probe function, which can be facilitated by minimizing aberrations using the data acquisition strategy described in fig. S3.

Unambiguous identification of O in the zeolite framework requires a resolution near 1 Å and good image contrast, which is rarely achievable with iDPC-STEM, given its sensitivity to sample thickness and time-constrained focusing unless the specimen is extremely thin (*20*). The iDPC-STEM image taken from ~40-nm-thick ZSM-5 did not match the [010]-projected structural model and is difficult to interpret (fig. S4), which is consistent with the simulation. When the imaging was performed on the crystal periphery, where the thickness was ~10 nm, the acquired iDPC-STEM image revealed 5-, 6-, and 10-membered rings (MRs) surrounded by T atoms; however, the O atoms located between the T atoms remained unresolvable (Fig. 1B).

In the ptychographic phase image of ~40-nm-thick ZSM-5 (Fig. 1C), all of the framework atoms, including O atoms, are unequivocally resolved. This image exhibited high precision in matching the projected structural model (Fig. 1D) with structural information transferred up to 0.85 Å, as determined from its Fourier transform pattern (fig. S5). By comparison, the highest resolution achieved in the STEM imaging of zeolites in the past was ~1 Å (*31*). Notably, the 4D-STEM data were collected at a high magnification after only coarse focusing at low magnification. Ptychography reconstruction revealed that the electron probe was ~35-nm defocused (fig. S6), which could not provide atomic resolution using conventional STEM modes. For beam-sensitive materials, an advantage of 4D-STEM ptychography is not needed to fine-tune the beam focus.

Similar results were obtained when ZSM-5 was imaged along the [100] axis. Thin specimens in this orientation were obtained by crushing commercial micrometer-sized ZSM-5 crystals into small fragments. Although the exact specimen thicknesses were unknown, we selected the highest-quality iDPC-STEM and ptychographic images obtained for comparison (Fig. 2, A and B). In this projection, four closely spaced T atomic columns (T-T distances: 0.8 to 1.8 Å; Fig. 2C) were indiscernible in the iDPC-STEM image (Fig. 2A) but were clearly separated in the ptychographic image (Fig. 2B), owing to the higher resolution achieved by ptychography compared with iDPC-STEM (fig. S5). The separation of these four atomic columns had not previously been achieved by imaging. When used for other types of zeolites—such as EMM-17, which has unusual 11-MR channels—4D-STEM ptychography also demonstrated higher resolution than iDPC-STEM and the ability to identify framework O atoms (Fig. 2, D to F).

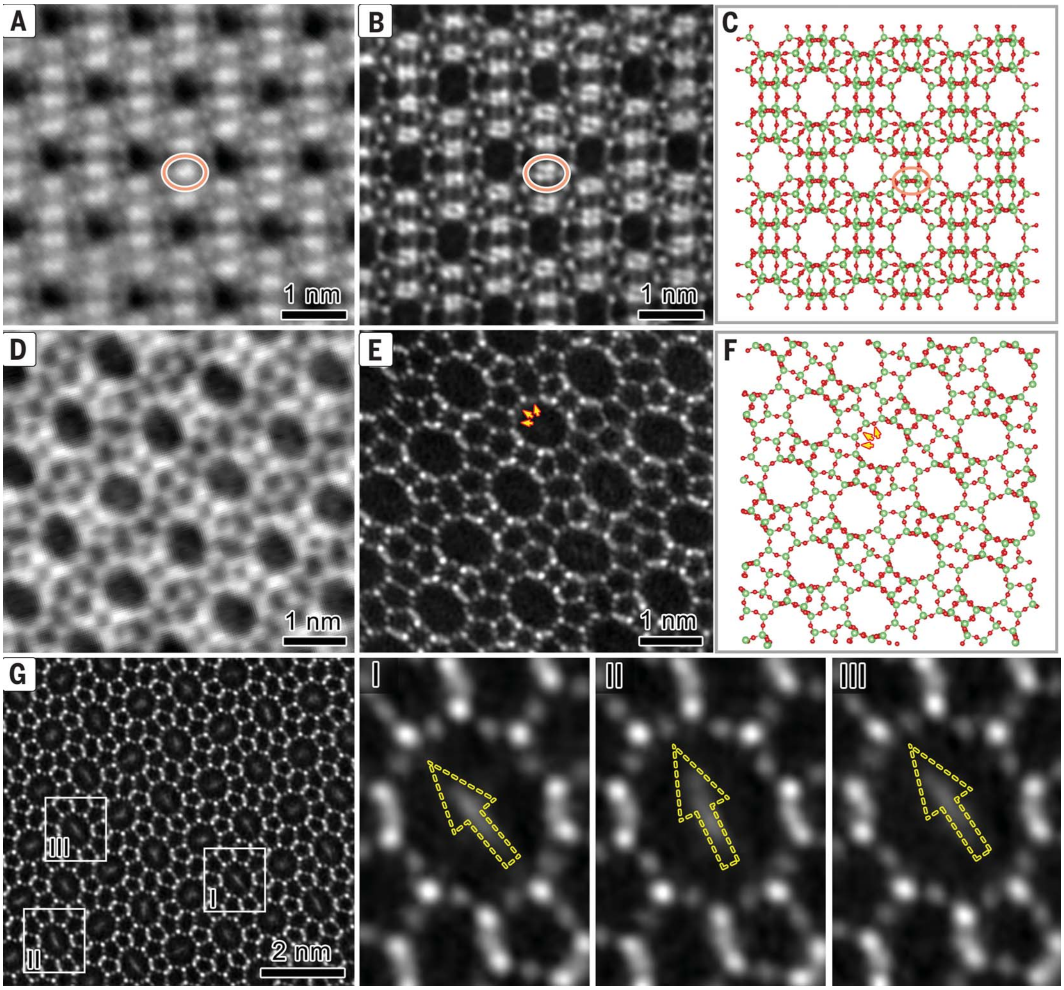

Fig. 2. Subangstrom imaging of zeolites and adsorbates using 4D-STEM ptychography. (**A** and **B**) iDPC-STEM (A) and 4D-STEM (B) ptychography images of ZSM-5 along the [100] axis. (**C**) The [100]-projected structural model of ZSM-5. The orange ellipses in (A) to (C) highlight the same positions, where four closely spaced columns of T atoms are resolved in (B) but not in (A). (**D** and **E**) iDPC-STEM (D) and 4D-STEM (E) ptychography images of EMM-17 along the characteristic 11-MR channel direction (i.e., the [001] axis). (**F**) The [001]-projected structural model of EMM-17. The yellow arrows in (E) and (F) indicate several O atomic columns in the framework, which are not resolved in (D). (**G**) 4D-STEM ptychographic image of ZSM-5 with adsorbed PX molecules along the straight 10-MR channel (i.e., the [010] axis). The square regions labeled I, II, and III are enlarged on the right to reveal the subtly different orientations of the PX molecules, as reflected by the rod-like contrast in the channels. The arrows are used as visual guides.

Resolving adsorbed molecules and oxygen vacancies

We used 4D-STEM ptychography to image ZSM-5 with adsorbed *p*-xylene (PX) molecules. The reconstructed ptychographic image displays rod-like and dot-like contrasts within the straight 10-MR channels (Fig. 2G), which are typically interpreted as adsorbed aromatic molecules in vertical and nearly horizontal configurations, respectively (*19*, *32*). However, the dot-like contrast is likely caused by the projection effect that results from the presence of multiple vertically adsorbed PX molecules with varying in-plane orientations. Whereas previous studies have reported similar observations using iDPC-STEM (*19*, *32*), the ultrahigh spatial resolution of 4D-STEM ptychography allows for more precise determination of the molecular orientations. As shown in Fig. 2G, the PX molecules pointing to the T atom, the O atom, and the middle of the T–O bond were all identified. The diverse orientations of adsorbed molecules imply the presence of complex host-guest interactions in zeolites that are caused by their inhomogeneous chemical environments.

Interestingly, we observed that the 10-MR channels with rod-like contrast displayed a more elongated shape (higher ellipticity) compared with those with dot-like contrast (fig. S7). This finding suggests that ZSM-5 has a flexible framework that can undergo local deformation in response to guest-molecule adsorption. However, we also noted the coexistence of 10-MR channels with markedly different ellipticities in pristine ZSM-5 without any adsorbates (fig. S8). Thus, although the the observation of inhomogeneous channel shape in ZSM-5 is intriguing, a definitive causal relationship between channel shape and molecular orientation has yet to be established.

Zeolites have Brönsted and Lewis acidity, both of which play vital roles in catalysis. The O vacancies generated by framework dehydration during high-temperature calcination is generally considered to be a major source of Lewis acidity, whereas direct observation of O vacancies in zeolites has not been realized to date. The ability of 4D-STEM ptychography to image O atomic columns in the zeolite framework also enabled the identification of O vacancies. To demonstrate this application, we collected 4D-STEM data from a ZSM-5 sample with a Si/Al ratio of ~100 along the [010] axis and reconstructed its phase image using the multislice ptychography method described above. The reconstruction result consists of seven slices, each with a thickness of 4 nm (two unit cells); thus, the imaged area is ~28 nm thick. We precisely identified the T and O atomic columns in each slice using an image-recognition software (see fig. S9), which were subsequently used for intensity analysis.

The intensity distribution of T columns plotted from the experimental ptychographic image was consistent with the simulation based on the defect-free ZSM-5 structure, both of which displayed a 3% coefficient of variation (Fig. 3A). By contrast, the O columns in the experimental ptychographic image exhibited a more pronounced intensity fluctuation than the simulation result (coefficient of variation: 7 versus 5%; Fig. 3B), suggesting the presence of O vacancies in the actual sample.

To explore the effect of O vacancies on the intensity of O columns, we performed image simulations using a series of [010]-projected ZSM-5 structural models, which were 4 nm

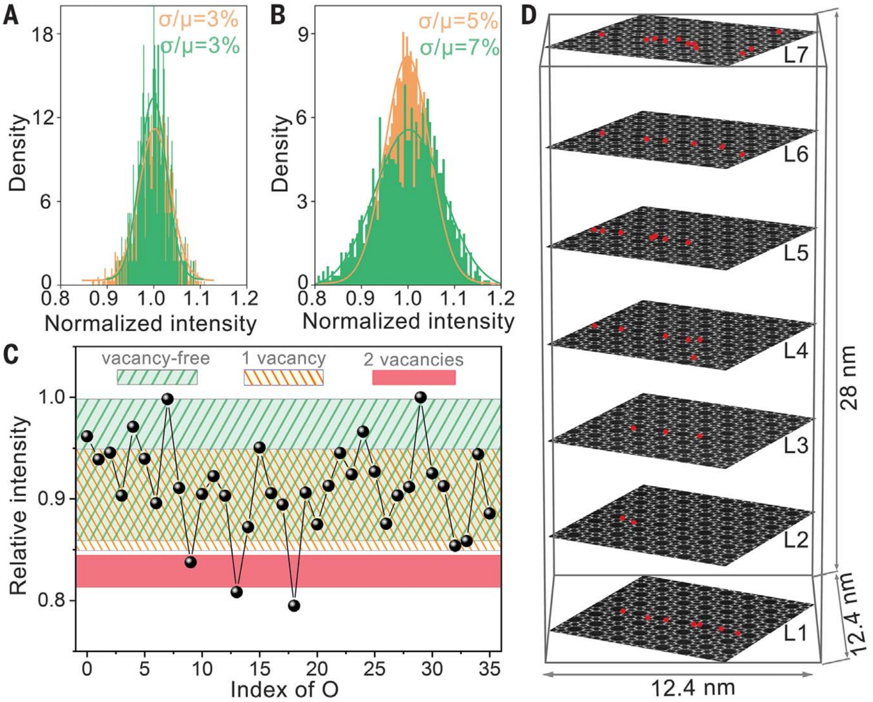

Fig. 3. Identification of O vacancies in ZSM-5. (**A** and **B**) Intensity histograms of T columns (A) and O columns (B) in the experimental (green) and simulated (orange) ptychographic phase images; σ is the standard deviation, and μ is the mean. The intensities are normalized by μ. The statistics are based on more than 1000 atoms. (**C**) Intensity variation of 36 O columns in the experimental ptychographic images. The image with the atomic index is presented in fig. S10. The intensity of each column is normalized by the maximum intensity in the 1-nm range. The light green region represents the intensity range of the O columns in the simulated ptychographic image using a vacancy-free model. The light yellow and red regions mark the intensity ranges of O columns that contain one and two O vacancies within a thickness of 4 nm, respectively. The model used for simulation is presented in fig. S11, and the intensity data are listed in table S1. In the experimental images, the columns with an intensity less than than the lower bound of the red region are identified as vacancy-containing columns. (**D**) Distribution of O vacancies identified by this method throughout the investigated region. The red dots represent identified columns containing O vacancies. L1 to L7 refer to layer 1 to layer 7.

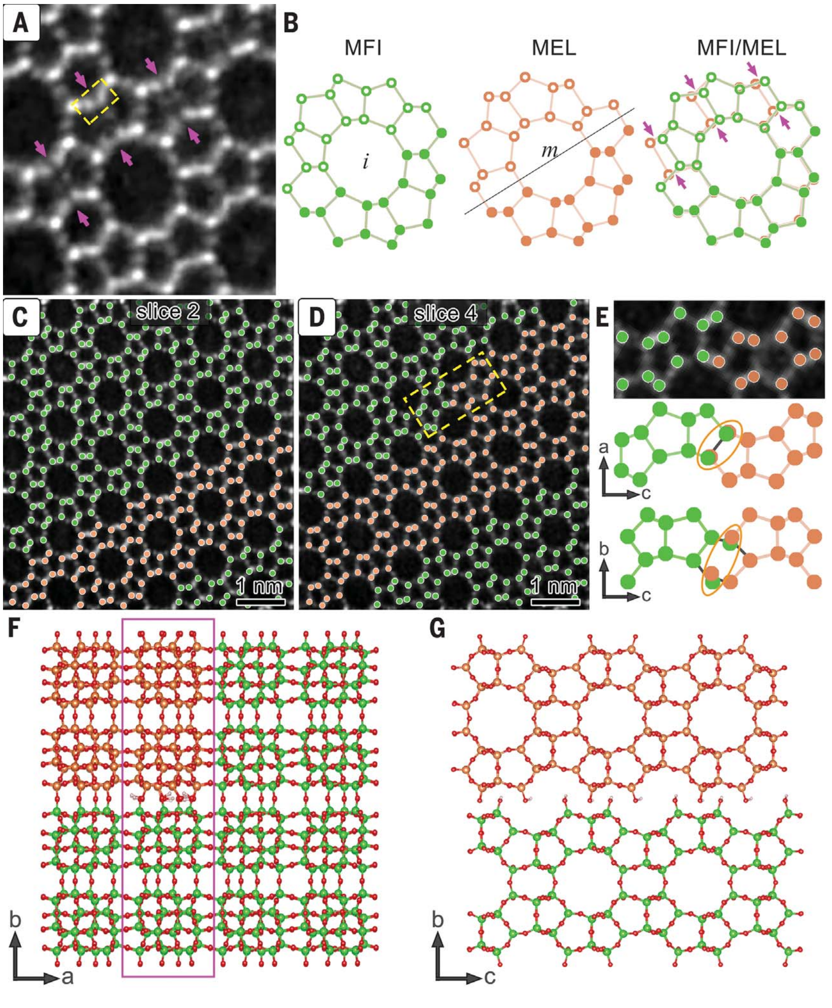

Fig. 4. Intergrowth of MFI and MEL phases in three dimensions. (**A**) 4D-STEM ptychography image displaying extra T atoms (indicated by the magenta arrows) relative to the typical MFI framework. The yellow dashed rectangle indicates the region analyzed in Fig. 5A. (**B**) Structural projections of straight 10-MR channels of MFI and MEL and their superposition. The letters *i* and *m* denote inversion and mirror symmetry, respectively. (**C** and **D**) Second (C) and fourth (D) slices of the multislice ptychography reconstruction result. Raw images are provided in fig. S16. The entire reconstructed volume is presented in movie S1 to display slice-by-slice structural changes. (**E**) At the top is an enlarged image from the region in (D) outlined by the yellow dashed rectangle, which shows the interface of MFI and MEL within the pentasil chain. The middle and bottom panels show a structural model of the interface that is viewed along different orientations, in which T atoms of MFI and MEL are all kept at the interface to demonstrate minimal mismatch. The ellipses highlight the columns at the interface. (**F**) Structural model of MFI-MEL intergrowth projected along the *c* axis. (**G**) The region enclosed by the magenta rectangle in (F) projected along the *a* axis, displaying the disconnected silanol-terminated interface perpendicular to the *b* axis. In (F) and (G), red and pink spheres represent O and H atoms, respectively. Green and orange spheres represent T atoms in MFI and MEL, respectively.

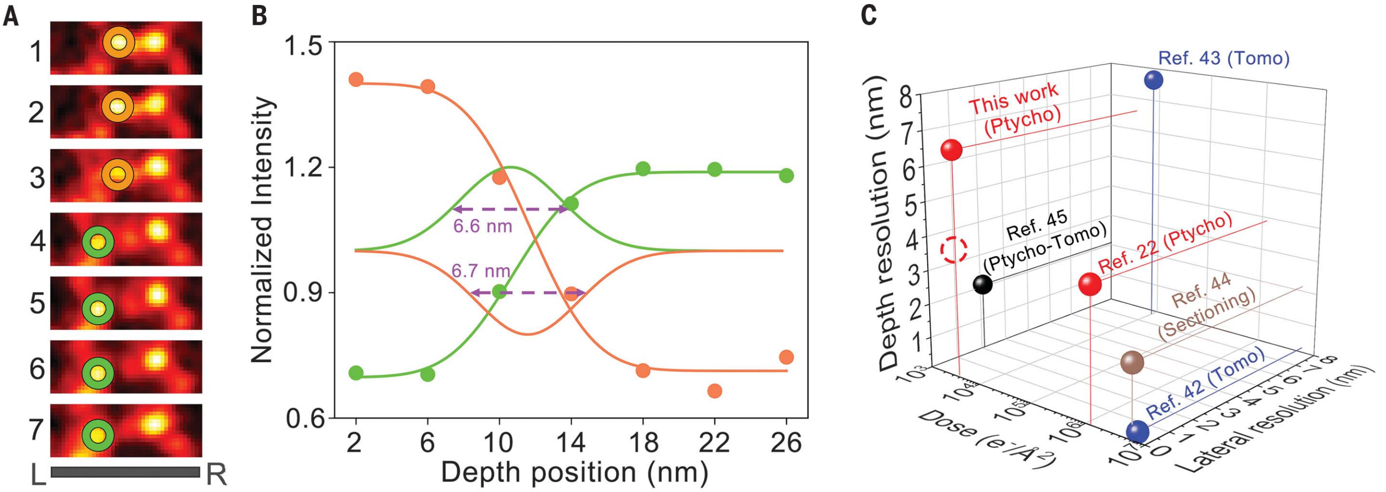

Fig. 5. Depth resolution achieved by 4D-STEM ptychography imaging of zeolites. (**A**) Slice-by-slice analysis of the region highlighted by the yellow dashed rectangle in Fig. 4A. Each slice is 4 nm thick. The green and orange circles mark the T columns in MFI and MEL, respectively. (**B**) Depth resolution estimation based on intensity profiles. Normalized intensities at the two locations indicated by the green and orange circles in (A) were extracted from seven successive slices and plotted as a function of their depth positions. The intensities were normalized by their mean values. The intensity variations at the two locations, represented by green and orange dots, are fitted with the error function. The full width at half maximum of the derivative (dashed lines) of the fitted error function is defined as the depth resolution. (**C**) Lateral and depth resolution reported for various 3D electron microscopy imaging methods. Tomo, Sectioning, Ptycho, and Ptycho-Tomo denote tomography, high-angle annular dark-field STEM depth sectioning, ptychography, and ptychographic tomography, respectively. The red dashed circle indicates the depth resolution of the ptychographic phase image that was reconstructed from a simulated 4D-STEM dataset.

thick and contained eight O sites in each O column, with varying degrees of O vacancy. The results indicated that one O vacancy within a thickness of 4 nm could not be reliably determined because the intensity reduction it caused was within the intrinsic intensity fluctuation of ZSM-5. When two or more aligned O vacancies were within a thickness of 4 nm, the resulting intensity reduction was sufficient for a reliable assignment (Fig. 3C).

We analyzed the ptychographic image of the ~28-nm-thick ZSM-5 slice by slice to render a 3D distribution of O vacancies within the crystal (Fig. 3D and fig. S12). Based on the simulation results (Fig. 3C), we established a relative intensity threshold of 81% to identify O vacancies. The result revealed that the imaged region of the zeolite contained a O vacancy concentration of ~51 μmol/g, with 58% of these O vacancies exposed to the straight 10-MR channels (table S2). It should be noted that the concentration of O vacancies obtained using this method needs to be treated with caution and preferably confirmed by other characterization techniques because the result is sensitive to the choice of intensity threshold. For instance, if a relative intensity threshold of 80% is chosen, the concentration of O vacancies is ~24 μmol/g (fig. S13). Probe-assisted nuclear magnetic resonance (*33*–*35*) and infrared spectroscopy of adsorbed pyridine (Py-IR) (*36*, *37*) are commonly used techniques for identifying and quantifying Lewis acid sites in zeolites that are closely related to O vacancies. The Py-IR method was used to determine the concentration of Lewis acid sites in the investigated ZSM-5 sample. The resulting value was ~35 μmol/g (fig. S14), which is in reasonable agreement with the concentration of O vacancies determined by 4D-STEM ptychography.

Intergrowth of MFI and MEL zeolites

Diffraction-based characterizations have revealed that ZSM-5 and ZSM-11 often coexist in synthetic products because they are similar in topology (MFI and MEL, respectively) (*38*, *39*). However, it is challenging to determine the exact coexistence state, such as whether they are mixed or intergrown, and how the minor phase is distributed relative to the major phase. The only direct evidence for the intergrowth of MFI and MEL by electron microscopy was obtained from a 2D single–unit cell–thick zeolite membrane, in which the two phases were interconnected along the *a* axis of MFI, forming an interface parallel to its *c* axis (*40*). However, conventional electron microscopy imaging has insufficient resolving power in the depth direction to explore the 3D intergrowth of zeolite crystals.

We demonstrate that electron ptychography provides a solution to this problem through the use of a zeolite material containing a primary phase, MFI, and concomitant phase, MEL, with an overall Si/Al ratio of ~90 (see materials and methods for the synthesis method). A comparison between experimental powder x-ray diffraction (PXRD) and PXRD simulation based on random-stacking disorder (*41*) indicated that MEL constitutes 10 to 20% in the material (fig. S15). The 4D-STEM ptychographic image of this material revealed subtle deviations from the typical structural projection along the MFI *b* axis, where there appeared to be some extra T atoms in the pentasil chain (Fig. 4A). The identification of extra T atoms indicated the presence of another structure besides MFI in the projection direction. Based on the PXRD results, we speculated that the imaged zeolite crystal contained MFI and MEL structures along the MFI *b* axis. The two structures of the pentasil family differ only in how the pentasil layers are connected (inversion symmetry for MFI versus mirror symmetry for MEL), and their stacking along the *b* axis resulted in a perfect match of the structure projection to the ptychographic image (Fig. 4B).

Because the reconstructed ptychographic image consisted of seven 4-nm-thick slices, a careful slice-by-slice analysis allowed us to confirm the intergrowth of MFI and MEL along the *b* axis while probing their interfaces in the *a-c* plane at atomic resolution (movie S1). In the first two slices, a narrow MEL domain consisting of only two pentasil chains was observed, sandwiched by MFI domains (Fig. 4C). In the fourth slice, the MEL domain expanded, resulting in the generation of a new MFI-MEL interface within the pentasil chain (Fig. 4D). These observations confirmed that MEL and MFI structures were intertwined in three directions within the crystal. Figure 4, C and D, displays how MFI and MEL structures were interconnected in the *a*-*c* plane. Along the *a* axis, the two structures were perfectly interconnected by sharing a pentasil chain without generating strain or defects, which was consistent with the previous observation (*40*).

The connection of the two structures along the *c* axis (that is, within the pentasil chain) could adopt three possible configurations (fig. S17), of which the one with the least interfacial mismatch was observed (Fig. 4E). Although the MFI-MEL interface perpendicular to the *b* axis could not be directly observed from ptychography given the limited depth resolution, it could be deduced based on the determined orientation relationship. When viewed along the *c* axis, the interface displayed alternating "connected" and "disconnected" regions along the *a* axis, each with a width of one-half the unit cell parameter *a* (Fig. 4F and fig. S18). The disconnected interface could not accommodate additional TO_4 tetrahedra and should be terminated by dangling silanol groups (Fig. 4G).

Depth-resolution analysis

The depth resolution of 4D-STEM ptychography, which is affected by imaging conditions and reconstruction parameters, must be determined explicitly for a given system. Using the 4D-STEM data acquired in this study and the LSQ-ML multislice algorithm, the minimum slice thickness for stable reconstruction was 4 nm, which defined the upper limit of depth resolution. The distinct structures of the two slices separated by 8 nm demonstrate a depth resolution better than 8 nm. To more precisely determine the depth resolution, we analyzed the intensity variation of two T atomic columns in seven consecutive slices spanning from one side of the MEL-MFI interface to the other, where the two studied columns were from MEL and MFI (Fig. 5A). In the interface region (i.e., slices 3 and 4), the two columns interfered in intensity because of the limited depth resolution (Fig. 5A). The two intensity profiles were fitted with error functions and their derivative curves were then derived (Fig. 5B). The full width at half maximum of the derivative curve, which is generally defined as the depth resolution, was measured as ~6.6 nm (Fig. 5B). By using a 4D-STEM dataset simulated at a total electron dose of ~3500 $e^-/\text{Å}^2$, a better depth resolution of ~3.5 nm could be achieved based on the same determination method because of the absence of experimental errors (fig. S19).

We compared the results of 4D-STEM ptychography in this study with previous results obtained using various 3D imaging methods in terms of lateral resolution, depth resolution, and consumed electron dose (Fig. 5C). Electron tomography can provide atomic resolution in three dimensions (*42*, *43*). Optical sectioning with high-angle annular dark-field STEM can generate subnanometer depth resolution with dense focal series (*44*). However, these two methods require very high electron doses, typically millions of $e^-/\text{Å}^2$, and are unsuitable for beam-sensitive materials (Fig. 5C and table S3). Ptychographic tomography exhibited ~2-nm resolution in three dimensions at low-dose conditions (Fig. 5C) (*45*).

Discussion

This study demonstrated that 4D-STEM multislice ptychography represents an efficient low-dose 3D imaging technique that exhibits excellent tolerance to the specimen thickness while not requiring precise focusing. These advantages make 4D-STEM multislice ptychography broadly applicable and particularly useful for imaging beam-sensitive materials. The lateral and depth resolutions achieved in this study are ~0.85 Å and ~6.6 nm, respectively, using a total electron dose of ~3500 $e^-/\text{Å}^2$. This performance has enabled an investigation of the intrinsic structural and compositional inhomogeneity in zeolites, including guest-molecule orientations, O vacancies, and multiphase intergrowth. The simulations indicate that under the imaging conditions that were used, the depth resolution can, in principle, be improved to ~3.5 nm. We believe that combining multislice ptychography with tomography is worth exploring because of its potential to further enhance 3D resolution.

REFERENCES AND NOTES

1. Y. Zhou *et al.*, *Science* **373**, 315–320 (2021).
2. Y. Li, J. Yu, *Nat. Rev. Mater.* **6**, 1156–1174 (2021).
3. M. Y. Jeon *et al.*, *Nature* **543**, 690–694 (2017).
4. K. Varoon *et al.*, *Science* **334**, 72–75 (2011).
5. D. E. Perea *et al.*, *Nat. Commun.* **6**, 7589 (2015).
6. S. M. Maier, A. Jentys, J. A. Lercher, *J. Phys. Chem. C* **115**, 8005–8013 (2011).
7. M. Ravi, V. L. Sushkevich, J. A. van Bokhoven, *Nat. Mater.* **19**, 1047–1056 (2020).
8. X. Liu *et al.*, *Angew. Chem. Int. Ed.* **60**, 24227–24233 (2021).
9. Q. Yu, X. Tang, H. Yi, *Chem. Eng. J.* **314**, 212–222 (2017).
10. T. Willhammar *et al.*, *Nat. Chem.* **4**, 188–194 (2012).
11. V. L. Zholobenko, M. A. Makarova, J. Dwyer, *J. Phys. Chem.* **97**, 5962–5964 (1993).
12. H.-M. Kao, C.-Y. Yu, M.-C. Yeh, *Microporous Mesoporous Mater.* **53**, 1–12 (2002).
13. W. Yuan *et al.*, *Science* **371**, 517–521 (2021).
14. L. Liu *et al.*, *Nat. Catal.* **3**, 628–638 (2020).
15. X. Li *et al.*, *J. Am. Chem. Soc.* **141**, 12021–12028 (2019).
16. D. Zhang *et al.*, *Science* **359**, 675–679 (2018).
17. K. C. Bustillo *et al.*, *Acc. Chem. Res.* **54**, 2543–2551 (2021).
18. L. Liu *et al.*, *Angew. Chem. Int. Ed.* **59**, 819–825 (2020).
19. H. Xiong *et al.*, *Science* **376**, 491–496 (2022).
20. B. Shen *et al.*, *Nature* **592**, 541–544 (2021).
21. Y. Jiang *et al.*, *Nature* **559**, 343–349 (2018).
22. Z. Chen *et al.*, *Science* **372**, 826–831 (2021).
23. G. Li, H. Zhang, Y. Han, *ACS Cent. Sci.* **8**, 1579–1588 (2022).
24. C. Ophus, *Microsc. Microanal.* **25**, 563–582 (2019).
25. T. J. Pennycook *et al.*, *Ultramicroscopy* **151**, 160–167 (2015).
26. C. M. O'Leary *et al.*, *Appl. Phys. Lett.* **116**, 124101 (2020).
27. M. Odstrčil, A. Menzel, M. Guizar-Sicairos, *Opt. Express* **26**, 3108–3123 (2018).
28. K. Wakonig *et al.*, *J. Appl. Crystallogr.* **53**, 574–586 (2020).
29. A. M. Maiden, M. J. Humphry, J. M. Rodenburg, *J. Opt. Soc. Am. A Opt. Image Sci. Vis.* **29**, 1606–1614 (2012).
30. S. Cao, P. Kok, P. Li, A. M. Maiden, J. M. Rodenburg, *Phys. Rev. A* **94**, 063621 (2016).
31. B. Shen *et al.*, *Adv. Mater.* **32**, e1906103 (2020).
32. B. Shen *et al.*, *Nature* **607**, 703–707 (2022).
33. J. H. Lunsford, W. P. Rothwell, W. Shen, *J. Am. Chem. Soc.* **107**, 1540–1547 (1985).
34. A. Zheng, S.-B. Liu, F. Deng, *Chem. Rev.* **117**, 12475–12531 (2017).
35. X. Yi *et al.*, *J. Am. Chem. Soc.* **140**, 10764–10774 (2018).
36. M. Guisnet, P. Ayrault, J. Datka, *Pol. J. Chem.* **71**, 1455–1461 (1997).
37. J. Zhang *et al.*, *ACS Catal.* **13**, 3794–3805 (2023).
38. G. R. Millward, S. Ramdas, J. M. Thomas, M. T. Barlow, *J. Chem. Soc. Faraday Trans. II* **79**, 1075–1082 (1983).
39. P. M. Piccione, M. E. Davis, *Microporous Mesoporous Mater.* **49**, 163–169 (2001).
40. P. Kumar *et al.*, *Nat. Mater.* **19**, 443–449 (2020).
41. M. M. J. Treacy, J. M. Newsam, M. W. Deem, *Proc. R. Soc. London Ser. A* **433**, 499–520 (1991).
42. M. C. Scott *et al.*, *Nature* **483**, 444–447 (2012).
43. D. Chen, H. Friedrich, G. de With, *J. Phys. Chem. C* **118**, 1248–1257 (2014).
44. R. Ishikawa, N. Shibata, T. Taniguchi, Y. Ikuhara, *Phys. Rev. Appl.* **13**, 034064 (2020).
45. Z. Ding *et al.*, *Nat. Commun.* **13**, 4787 (2022).
46. H. Zhang *et al.*, Data Set: Three-dimensional structural and compositional inhomogeneity in zeolites unraveled by low-dose electron ptychography. KAUST Repository (2022); https://repository.kaust.edu.sa/handle/10754/690886.

ACKNOWLEDGMENTS

We acknowledge the KAUST Supercomputing Laboratory for providing the computing resources, J. H. Xin for assistance in setting up the computing environment, and F. Lin and P. Pelz for discussions on ptychography. **Funding:** This work was funded by the National Key Research and Development Project of China (2022YFE0113800), the KAUST Center Competitive Fund (FCC/1/1972-43-01), Liaoning Revitalization Talents Program (XLYC2008032), and Fundamental Research Funds for the Central Universities (DUT22LAB602). **Author contributions:** Conceptualization: Y.H., H.Z.; Methodology: H.Z., G.L., Z.C., J.Z., X.L., C.C., Y.Z.; Investigation: Y.H., H.Z., G.L., J.Z., L.L.; Visualization: H.Z., G.L., D.Z., Y.Z.; Supervision: Y.H., H.Z., X.G., D.Z., P.G.; Writing – original draft: H.Z.; Writing – review and editing: Y.H., G.L., C.C., P.G., X.G., Z.C. **Competing interests:** The authors declare no competing interests. **Data and materials availability:** All data needed to evaluate the conclusions in the paper are present in the paper and the supplementary materials. The original image data are available at the KAUST Repository (*46*).

SUPPLEMENTARY MATERIALS

science.org/doi/10.1126/science.adg3183
Materials and Methods
Figs. S1 to S19
Tables S1 to S3
References (*47*–*52*)
Movie S1

Submitted 15 December 2022; accepted 5 April 2023
10.1126/science.adg3183

Three-dimensional inhomogeneity of zeolite structure and composition revealed by electron ptychography

Hui Zhang, Guanxing Li, Jiaxing Zhang, Daliang Zhang, Zhen Chen, Xiaona Liu, Peng Guo, Yihan Zhu, Cailing Chen, Lingmei Liu, Xinwen Guo, and Yu Han

Science, **380** (6645), .
DOI: 10.1126/science.adg3183

Editor's summary

Zeolite structures are prone to structural and compositional inhomogeneities that can cause batch-to-batch variations in applications. However, imaging these variations is difficult in transmission electron microscopy (TEM) because zeolites are prone to electron beam damage at the doses needed for atomic resolution. Zhang *et al*. found that electron ptychography based on low-dose four-dimensional scanning TEM data could achieve subangstrom resolution. The authors resolved individual oxygen atom columns in various zeolites with specimen thicknesses of up to 40 nanometers and mapped the distribution of oxygen vacancies throughout a zeolite. Complex intergrown structures between different zeolite phases were also imaged. —Phil Szuromi

Science (ISSN) is published by the American Association for the Advancement of Science. 1200 New York Avenue NW, Washington, DC 20005. The title *Science* is a registered trademark of AAAS.